



Bottom-Up-Etching Mediated Synthesis of Large-Scale Pure Monolayer Graphene on Cyclic-Polishing-Annealed Cu(111)

Yao, Wenqian; Zhang, Jianing; Ji, Jie; Yang, He; Zhou, Binbin; Chen, Xin; Bøggild, Peter; Jepsen, Peter Uhd; Tang, Jilin; Wang, Fuyi

Total number of authors:
15

Published in:
Advanced Materials

Link to article, DOI:
[10.1002/adma.202108608](https://doi.org/10.1002/adma.202108608)

Publication date:
2022

Document Version
Peer reviewed version

[Link back to DTU Orbit](#)

Citation (APA):

Yao, W., Zhang, J., Ji, J., Yang, H., Zhou, B., Chen, X., Bøggild, P., Jepsen, P. U., Tang, J., Wang, F., Zhang, L., Liu, J., Wu, B., Dong, J., & Liu, Y. (2022). Bottom-Up-Etching Mediated Synthesis of Large-Scale Pure Monolayer Graphene on Cyclic-Polishing-Annealed Cu(111). *Advanced Materials*, 34(8), Article e2108608. <https://doi.org/10.1002/adma.202108608>

General rights

Copyright and moral rights for the publications made accessible in the public portal are retained by the authors and/or other copyright owners and it is a condition of accessing publications that users recognise and abide by the legal requirements associated with these rights.

- Users may download and print one copy of any publication from the public portal for the purpose of private study or research.
- You may not further distribute the material or use it for any profit-making activity or commercial gain
- You may freely distribute the URL identifying the publication in the public portal

If you believe that this document breaches copyright please contact us providing details, and we will remove access to the work immediately and investigate your claim.



Pushing the boundaries
of chemistry?
It takes
#HumanChemistry

Make your curiosity and talent as a chemist matter to the world with a specialty chemicals leader. Together, we combine cutting-edge science with engineering expertise to create solutions that answer real-world problems. Find out how our approach to technology creates more opportunities for growth, and see what chemistry can do for you at:

evonik.com/career

 **EVONIK**
Leading Beyond Chemistry

Bottom-Up-Etching Mediated Synthesis of Large-Scale Pure Monolayer Graphene on Cyclic-Polishing-Annealed Cu(111)

Wenqian Yao^{1,2,†}, Jianing Zhang^{1,2,†}, Jie Ji³, He Yang¹, Binbin Zhou⁴, Xin Chen³, Peter Bøggild³, Peter U Jepsen⁴, Jilin Tang⁵, Fuyi Wang⁵, Li Zhang⁶, Jiahui Liu⁶, Bin Wu^{1,*}, Jichen Dong^{1,*}, and Yunqi Liu^{1,2,*}

[†]These authors contributed equally to this work.

W. Q. Yao, J. N. Zhang, Dr. H. Yang, Prof. B. Wu, Prof. J. C. Dong, Prof. Y. Q. Liu

Beijing National Laboratory for Molecular Sciences

Key Laboratory of Organic Solids

Institute of Chemistry, Beijing 100190, P. R. China

E-mail: wubin@iccas.ac.cn; dongjichen@iccas.ac.cn; liuyq@iccas.ac.cn

W. Q. Yao, J. N. Zhang, Prof. Y. Q. Liu

Sino-Danish Center for Education and Research, Sino-Danish College, University of Chinese Academy of Sciences, Beijing 100049, China.

Dr. J. Ji, Dr. X. Chen, Prof. P. Bøggild

Department of Physics, Technical University of Denmark, DK-2800 Kongens Lyngby, Denmark.

Dr. B. B. Zhou, Prof. P. U Jepsen

Department of Photonics, Technical University of Denmark, DK-2800 Kongens Lyngby, Denmark.

J. L. Tang, Prof. F. Y. Wang

Beijing National Laboratory for Molecular Sciences, National Centre for Mass Spectrometry in Beijing, CAS Key Laboratory of Analytical Chemistry for Living Biosystems, Institute of Chemistry, Chinese Academy of Sciences, Beijing, 100190, P. R. China.

This article has been accepted for publication and undergone full peer review but has not been through the copyediting, typesetting, pagination and proofreading process, which may lead to differences between this version and the [Version of Record](#). Please cite this article as [doi: 10.1002/adma.202108608](#).

J. H. Liu, L. Zhang

Analytical Instrumentation Center, College of Chemistry and Molecular Engineering, Peking University, Analytical Instrumentation Center, College of Chemistry and Molecular Engineering, Peking University, Beijing 100871, P. R. China.

Keywords: single-crystal Cu(111), monolayer graphene, chemical vapor deposition, grain boundary migration, etching

Abstract:

Synthesis of large-scale single crystalline graphene monolayer without multi-layers involves the fabrication of proper single crystalline substrates and the ubiquitous formation of multi-layered graphene islands during chemical vapor deposition. Here, we present a cyclic electrochemical polishing combined with thermal annealing method that allows the conversion of commercial polycrystalline Cu foils to single-crystal Cu(111) with an almost 100% yield. We demonstrate a global “bottom-up-etching” method that is capable of fabricating large area pure single crystalline graphene monolayer without multilayers through selectively etching bottom multi-layered graphene underneath large area as-grown graphene monolayer on Cu(111) surface. Terahertz time-domain spectroscopy (THz-TDS) measurement of pure monolayer graphene film shows a high average sheet conductivity of 2.8 mS and mean carrier mobility of $6903 \text{ cm}^2\text{V}^{-1}\text{s}^{-1}$ over large area. Density functional theory (DFT) calculations show that the selective etching is induced by the much easier diffusion of hydrogen atoms across the edges of the top graphene layer than hydrocarbon radicals, and the simulated selective etching processes based on phase field modelling are well consistent with experimental observations. This work provides new ways towards the production of single-crystal Cu(111) and the synthesis of pure monolayer graphene with high electronic quality.

1. Introduction

Synthesis of high-quality large-area single crystalline graphene monolayer is of critical importance for its vast practical applications as well as for investigating the fundamental physical

This article is protected by copyright. All rights reserved.

phenomena in 2D space based on graphene.^[1-3] Currently, seamless stitching of unidirectionally aligned graphene islands growing on a substrate has been realized in achieving this goal, while this kind of methods face two main challenges—(i) fabrication of a proper single crystalline substrate consistent with the symmetry of graphene to ensure the unidirectional alignment of graphene islands and (ii) avoiding the formation of multi-layers in the process of growing graphene monolayer samples.

Due to the C_{6v} symmetry of graphene, substrates showing one-, two-, three- and six-fold symmetries can in principle template the unidirectional growth of graphene islands during chemical vapor deposition (CVD).^[4,5] In practice, annealing of face-centered cubic (FCC) transition metals (TMs) predominantly leads to the appearance of six-fold symmetric (111) facets because of their lowest surface energies.^[6,7] Up to now, there have been mainly two types of methods of fabricating single crystalline FCC TM substrates with (111) facets, including the growth of thin TM films on single crystalline wafers^[6,7] and direct annealing of polycrystalline TM foils into single crystals^[8,9] such as temperature-gradient annealing using a delicate experimental setup,^[10,11] contact-free-annealing of polycrystalline Cu foils predominantly with {112}<111> grains,^[12] or thermal annealing of Cu foils with pre-formed single crystalline seeds.^[13] However, the mechanism of conversion is still largely unknown, and the complications of operation, equipment or the use of polycrystalline metal foils with specific textures involved in these studies also hinder widespread applications. Considering various pathways of poly- to single-crystal conversion inherently existing in this complex system, it is highly demanded to explore an effective and robust method for ease conversion and in-depth understanding of the mechanism.

During CVD growth of graphene on a single crystalline Cu(111) substrate, multi-layered graphene formed underneath the first layer is ubiquitous because of the non-uniform local environment or the existing of impurity particles that facilitate the nucleation and growth of the

graphene multi-layers.^[14-18] It was also found that crystalline facet orientations of the substrate and the carbon residues or contaminations on and inside the substrate also play critical roles in the formation of multi-layers.^[19] Cu(111) substrates were found to be superior as substrates to synthesize graphene monolayers with less multi-layers than Cu substrates with other facets.^[20] Pretreatment of substrates like reducing surface roughness by electrochemical polishing and carbon residues by high-temperature annealing in H₂ atmosphere for a long time have been revealed to be capable of lowering multi-layer coverage, while in practice there are always steps, kinks and impurity particles, especially SiO₂, on Cu substrates and thus multi-layers will form during CVD. Up to now, it is still unclear whether it is possible to minimize or completely eliminate the non-uniformity effect due to the existence of extra graphene multi-layers.

Here we demonstrate for the first time a cyclic electrochemical polishing combined with thermal annealing method that allows the production of single-crystal Cu(111) from commercial polycrystalline Cu foils with a size up to 4 × 32 cm², which is limited by the size of furnace tube. The conversion can be completed by 2–4 cycles with a yield of almost 100% within only 2–4 hours' annealing. Based on a collection of observations such as GB migration and grain size distribution, we propose that the conversion is a typical abnormal grain growth process and that cyclic electrochemical polishing can effectively remove the impurities that aggregate at the Cu grain boundaries (GBs) and pin their motions supported by experiments, which makes the complete conversion of polycrystalline Cu foils into single crystals possible. Moreover, we develop a global "bottom-up-etching" method that allows the synthesis of uniform monolayers of single-crystal graphene on the obtained single crystalline Cu(111) foils. This method is based on the key finding that the etching of multi-layers underneath the graphene monolayer film is layer-dependent with the faster etching rate for the underlying graphene multi-layers by slightly decreasing the supply of methane after the full coverage of graphene during CVD. Pure monolayer graphene film shows a high average sheet conductivity of 2.8 mS and carrier mobility of 6903 cm²V⁻¹s⁻¹ over large area up to 17

This article is protected by copyright. All rights reserved.

cm² measured by THz-TDS technique. Our DFT calculations reveal that decreasing the supply of methane can lead to a near-equilibrium condition for the top-layer graphene film and simultaneously result in the etching of bottom multi-layers, because of the much easier diffusion of etchant hydrogen atoms into the interface between substrate and the first graphene layer via graphene edges than that of hydrocarbon radicals. In addition, phase field simulations of the selective etching of bottom layers based on this understanding are well-consistent with experimental observations, which further proves our proposed mechanism on the selective etching method. This work makes a contribution to the low-cost and high-yield production of single-crystal Cu(111) foils and the precise control of large-scale single crystalline graphene layer uniformity.

2. Results

2.1 Synthesis and characterization of Cu(111)

Figure 1a shows schematic of our approach for producing single-crystal Cu(111) involving cyclic electrochemical polishing and thermal annealing processes (see also Methods). Typical optical and scanning electron microscopy (SEM) images of as-prepared Cu(111) foil are shown in **Figure 1b** and **1c**, respectively. The surface of large single-crystal Cu(111) appears smooth and flat, and shows uniform color contrast without the presence of GBs. **Figure 1d** shows a typical atomic force microscopic (AFM) image of as-prepared Cu(111) surface, which displays the characteristic three-directions associated with slip lines along $\langle 110 \rangle$ on Cu (111) surface.^[6,21] The X-ray diffraction (XRD) characterization (**Figure 1e**) on samples shows a sharp single high-intensity peak at 43.3° that is the characteristic peak of Cu(111). Inverse pole figure (IPF) maps (**Figure 1f**) from electron back-scattered diffraction (EBSD) recorded on different areas of an as-prepared Cu foil across the whole surface show homogeneous color, indicating highly-crystalline Cu(111) surface without the presence of subgrain boundaries. The corresponding pole figures (**Figure 1g**) and kernel average misorientation (KAM) maps (**Figure 1h**) demonstrate that as-prepared Cu (111) has the same in-plane orientation.

Cu(111) is also confirmed by high-resolution transmission electron microscope (TEM) characterization (Figure S1). The sizes of single-crystal Cu(111) foils are simply dependent on the furnace used (2-inch quartz tube in our case), and the repeated use of this method resulted in a single-crystal Cu(111) foil with a size up to $4 \times 32 \text{ cm}^2$ (Figure 1i).

In comparison, thermal annealing of polycrystalline Cu foils for a long time without electrochemical polishing essentially failed to produce large-scale Cu(111) foils (Figure S2), thus highlighting the critical role of electrochemical polishing and cyclic operation of Cu in the conversion. Investigating the whole process reveals several typical important points. First, in sharp contrast to very rough surface of commercial Cu foils (Figure 2a–c), the first polishing process results in a smooth and flat Cu surface (Figure 2d, e). This is due to the fact that a protrusion part on Cu surface is associated with a high electric field, causing a faster dissolution in electrochemical polishing process.^[22] Second, after the first annealing process with 1 h, Cu surface typically appears several emerging features such as the network of GBs with single domains from tens to hundreds of micrometer, bumps or thermal grooves with varied size (Figure 2f). Third, the second polishing is capable of erasing out these features, leading to an appearance similar to that of the first polishing (Figure 2g). However, GBs are still present, and most of bumps or grooves typically disappear after the second thermal annealing (Figure 2h). Note that GBs formed after annealing show a deep groove configuration with a height ranging from 100-400 nm (Figure 2i). Finally, Cu(111) foils can be obtained with 2–4 cycles (Figure 1).

2.2 Mechanism of the conversion from polycrystalline to single crystalline Cu(111)

To understand the mechanism of conversion, several key observables in this dynamic system including the change of GB location, GB flattening and merging were measured by combining optical imaging, SEM and EBSD measurements, which have been rarely reported. Figure 3a–c shows a typical movement of a GB during the process. Note that the sample was slightly oxidized in air at

200 °C for 2 min for optical imaging. Our experiments showed that different colors in Figure 3a are associated with different Cu grains that have different oxidization rates (Figure S3).^[23] This technique is capable of rapidly identifying grains, and positions of GBs before and after their movement. For example, adjacent light and dark lines indicating the possible positions of GBs can be found in the optical image in Figure 3a, which were also observed in the corresponding SEM image (Figure 3b). EBSD mapping in the same area confirms that the light and blue lines in Figure 3a actually denote the original and current positions of the GB (denoted by GB₁ and GB_{1'}), respectively (Figure 3c). Moreover, it can be seen that that Cu(111) grain is growing larger at the cost of adjacent Cu(110) grain, in which several speckles indicate the existence of small subgrains on Cu(110) (Figure 3c). The motion direction of this GB can also be identified, which is towards the center of GB curvature that is consistent with the growing direction of Cu(111), and the motion of a GB appears not uniform as evidenced by the two curved lines with different geometrical shapes (Figure 3a–c and Figure S4). A more complex case involving motions of interconnected GB lines is shown in Figure S5.

It should be noted that the motion direction of the GBs is determined by both surface energy of grains and the local curvature of GBs between grains. As schematics shown in the inset of Figure 3a, the energy change per unit volume after a small motion of a GB is:

$$dE = \frac{2\Delta\gamma r d\theta dr + \gamma_{GB} h d\theta dr}{h r d\theta dr} = \frac{2\Delta\gamma}{h} + \frac{\gamma_{GB}}{r}, \quad (1)$$

where $\Delta\gamma$ is the surface energy difference between the two grain facets, γ_{GB} is the GB energy, h represents the thickness of the Cu foil and $1/r$ is the local curvature of the GB, the coefficient 2 in the first term represents the two surfaces of the Cu foils. Eq. (1) shows that the motion of a GB is not necessarily towards the direction of surface energy decreasing ($\Delta\gamma < 0$), if the local curvature of the GB $1/r$ is negative. Indeed, we have observed the motion of a GB from a high-energy facet towards a low-energy one ($\Delta\gamma > 0$), which will be shown in the following discussion.

Previous studies have classified grain growth behaviors into two groups: normal grain growth (NGG) and abnormal grain growth (AGG), which is based on the criterion of how fast grain grows.^[24–27] Figure 3d–e demonstrates the evolution of grains for the same Cu area with the treatment of the second and third cycles, in which millimeter-scale AGG occurs. We found that there is no much change in the grain texture after the first two cycles of treatment around this area, where a large Cu(110) grain was on the left side and many small grains with different facets on the right side (Figure 3d, also see Figure S6 for the optical image of this area after the first cycle treatment). In contrast, after the third cycle, the whole Cu surface changes dramatically (Figure 3e). Specifically, the right region on Cu surface containing many different grains including Cu(111) appears the same color, indicating that this whole area becomes Cu(111), as driven by the lowest surface energy of Cu(111) and elimination of GBs. It is worth noting that the motion of GB from Cu(110) towards Cu(111) (denoted by blue and red arrows in Figure 3e), which is induced by the local negative curvature of the GB, can be explained above. More such examples are shown in Figure S7.

To reveal the conversion mechanism from polycrystalline Cu foils to single crystals by cyclic electrochemical polishing and annealing, statistics on the grain size within $4 \times 4 \text{ cm}^2$ area of a Cu foil under different treatment cycles are obtained, as shown in Figure 3f. It can be seen that the grain size increases significantly with the increase of treatment cycles. Moreover, the bimodal distributions suggest that the conversion is mediated by AGG. We propose that the cyclic electrochemical polishing removes impurity particles that accumulate at GBs in the Cu foil and pin their motion, which leads to the successful conversion of polycrystalline Cu foils to single crystals. Zener equation shows that the limiting size of the normal grains during annealing can be estimated by $\frac{\alpha}{f}$, where α is a parameter related to the diameter of impurity particles and f is the volume fraction of impurity particles.^[28] If we assume that only β percent of impurity particles is remained after one cycle of electrochemical polishing, then $f = f_0 \beta^N$ with f_0 to be the original volume fraction of impurity

particles and the size of the normal grains after the N th annealing cycle is $\frac{\alpha}{f_0\beta^N}$. Figure 3g shows the evolutions of the mean diameter of normal grains and the largest diameter of abnormal grains with the increase of treatment cycles N . Obviously, the mean diameter of normal grains increases exponentially with N , and β is fitted to be 0.43, which is strikingly consistent with our analysis. More importantly, we found that the size of the largest abnormal grain also satisfies the Zener prediction and increases exponentially with N and β is fitted to be 0.17. The smaller β for abnormal grains suggests their faster growth rates than normal ones and proves that polycrystalline Cu foils can always be annealed into single crystals by our method.

We have performed extensive experiments to investigate the impurity information of Cu before and after treatments including X-ray fluorescence (XRF), X-ray photoelectron spectroscopy (XPS) and time-of-flight secondary ion mass spectrometry (ToF-SIMS) techniques. Several impurity elements such as Al, Fe, Ca, Zn, S, Cl, Si and P with several hundred ppm level are detected in initial Cu foils by XRF measurements, among which Al and Fe elements are not found in treated Cu foils in XRF data, and the concentrations of Ca and Zn elements in single-crystal Cu foils are much lower than those of initial Cu (Table S1). XPS measurements of initial and treated Cu foils (Figure S8) show that only Al and Fe elements are absent, indicating that Al and Fe elements are from external contaminants. Moreover, the impurity concentrations of S, Cl and Si elements show a clear decreasing trend with the cycle number, strongly indicating that the impurities are removed by the treatment (Figure S9). Note that the impurity of P element essentially remains the same with a small fluctuation, possibly due to the fact that the electrochemical polishing solution contains phosphoric acid (Figure S8). Finally, impurity concentration distributions of Cl and P on Cu surface essentially map GB profiles by ToF-SIMS mappings of treated Cu foils (Figure S10), in which the concentrations of Cl along GBs are higher than those on surface with the highest contrast compared to P, Si and S mappings. Note that a fluctuation of element concentration distributions along GBs and grain surface can also be seen, and apparent “dark” regions along “light” lines is most likely from the effect of GB morphology. In a word,

This article is protected by copyright. All rights reserved.

these results are indeed consistent with the main points that impurities in Cu tend to accumulate in GB regions, and the impurities are removed by electrochemical polishing process.

In order to further reveal the mechanism of grain growth at microscopic scale, AFM imaging of GB locations was performed to characterize the morphological changes of GBs after their migration. Two locations in Figure 3h were highlighted. Marked areas covering the location of the original intersecting point (Figure 3i) show no detectable grooves or signals for the existence of GBs after their migration. For comparison, newly-formed GBs (Figure 3j) show typical GB morphology and grooves with a height range similar to that for original GB (Figure 2i). These results further demonstrate that grain growth process involves GB migration and the flattening steps.

With these collected observables in mind, it is possible to discuss the mechanism of grain growth in more details and establish a connection between microscopic motion of Cu atoms and global observations in the process. First, from the microscopic point of view, the existence of GBs causes a distortion of Cu lattice that is associated with a local energy field gradient. This gradient and surface energy difference provide driving forces for motion of adjacent Cu atoms, which is responsible for global grain growth. Using this picture, several basic observations or empirical rules can be well-explained. For example, stress/strain-induced energy field gradient or temperature-gradient enable other external driving forces for the conversion. Grain growth appears to occur by the motion of GBs. Considering high energy of GBs, local gradient drives the directional motion of local atoms, and this microscopic motion of atoms can equivalently be described by a global motion of GBs. In this sense, while net results allow various kinds of routes from the initial to final states, global atom plane rotation or translation are not energetically preferred. Moreover, local geometric features such as GB curvatures are directly associated with local distortion degree of Cu lattice, and thus eliminating or reducing the curvature of a GB curve is energetically preferred, leading to a

motion direction towards the center of a GB curvature and simultaneous minimization of the curvature of a GB.

Second, the observations or classifications of NGG and AGG modes appear to be related to the randomness of this complex process, which possibly originates from the lacking of detailed microscale information of starting Cu foils, or from the complex interaction of GBs motion during the conversion. This randomness has some consequences that can be observed. For example, it is difficult to predict when and how an AGG occurs (Figure S11 and S12), how many exact polishing cycles are required or how long every annealing time should be. As a result, these parameters are empirically determined, and may not be mostly optimized for certain case. Statistical results are very reliable regardless of these fluctuations in terms of cycle times, the starting or ending time of AGG, annealing duration and so on. On the other hand, AGG may be more likely a synergetic phenomenon, involving the interactions of many grain growths and GBs motions in which certain Cu(111) was randomly-selected to grow larger and then this growth dominates the neighboring grain growth. In practice, the best example can be realized by two cycles of polishing and annealing.

Finally, cyclic Cu polishing plays a critical role in Cu(111) foil production, which can remove contaminants and impurities on surface and GBs. Due to the high energy of GBs, impurities are readily diffused from the surface or segregated from the bulk to GB regions,^[29] which is not preferred for GB movement in both energetics and kinetics. Statistically, the requirement of Cu conversion is that a big number of energy values imputed into the system are factored into the addition of a large number of small energy costs. In this sense, an interconnected GB network in a polycrystalline material remains to be locked even when a small fractions of GBs are pinned by impurities. Considering the existence of various kinds of GBs^[30] (low-angle, large-angle, high-mobility, low-mobility, and so on) between different Cu grains, the grain growth can be terminated at some stages

or some locations. Our approach provides an effective response in a global and cyclic manner that minimizes this potential failure of grain growth.

2.3 Growth and characterization of single-crystal pure graphene monolayer

The development of the method of producing Cu(111) and deeper understanding of conversion mechanism allows the direct applications of our as-prepared Cu(111) foils to the CVD growth of graphene, which has been extensively investigated in recent years, as Cu(111) provides a symmetry and lattice-matched substrate for the formation of well-aligned graphene domains and their further coalescence into single crystalline films. These graphene films generally contain multi-layered graphene portions, the percentage and distribution of which are dependent on various experimental conditions. Traditional approach for restraining the possibility of multi-layered nucleation and growth is mainly based on controls over parameters such as C sources, carrier gas types, pressure, temperatures or substrates during the growth stage.^[31,32] However, the realization of a complete monolayer graphene growth on Cu(111) surface remains elusive at present.

To solve this issue, our general idea is not to control nucleation and growth stages of graphene, but to modulate etching process after the formation of multi-layered graphene films. Our approach involves a first graphene film growth stage and then a second “bottom-up-etching” stage that is capable of etching away the underlying multi-layers^[33-36,19] with the survival of the upper single-layer graphene (Figure S13). The experiments involving the use of $^{12}\text{CH}_4$ and $^{13}\text{CH}_4$ as graphene growth precursors (Figure S14), Raman spectroscopy (Figure S15) and oxygen plasma etching (Figure S16) were performed to determine whether the second layer grows below or above the first grown graphene monolayer, and we found that the former is indeed the case and consistent with previous studies. Briefly, during the first growth stage, a relatively large concentration of CH_4 was used to grow a common multi-layered graphene film on Cu(111) surface, and then the flow rate of CH_4 was reduced to a value at which as-grown upper single-layer graphene is non-etched, and the multi-

layered graphene under the first single layer can be gradually etched away. After a certain period of time, a uniform single crystalline monolayer graphene can be obtained (Figure S17). This idea provides a route for general and global controls of the complete monolayer graphene synthesis regardless of growth conditions and various non-uniformity of multi-layered samples.

Figure 4a shows a typical optical image of multi-layered graphene film synthesized during the first stage transferred onto a 300 nm SiO₂/Si substrate, in which many dark areas representing multi-layered portions are non-uniformly distributed on the continuous graphene film. In sharp contrast, as-grown graphene film shows a uniform color contrast, indicating a monolayer graphene film after the completion of the whole stages (Figure 4b). The zoom-in images of both samples in the inset of Figure 4a and 4b show characteristic optical contrast of multi-layer and monolayer graphene films, respectively. The comparison of Raman mappings of samples further confirms the nature of multi-layered graphene (Figure 4c and Figure S18a–c) and the uniformity of monolayer graphene over a large length scale (Figure 4d and Figure S18d–f), respectively. All Raman spectra of monolayer graphene film measured at different locations over an area of 17 cm² show the similar results, in which D band located at 1350 cm⁻¹ is absent or negligible, and the peak intensity ratios between 2D and G are about 1–3 (Figure 4e and Figure S18f), demonstrating that as-grown graphene films are uniform monolayer.

In order to further evaluate samples' electronic quality with a spatial resolution at a large-scale, THz-TDS measurements (See methods and Figure S19) were performed. Figure 4f and Figure S20a show DC sheet conductivity map and histogram of large-area graphene film with multi-layered coverage similar to the case in Figure 4a. For comparison, improved uniformity of DC sheet conductivity (2.8 mS) for monolayer graphene film can be directly visualized from Figure 4g. In addition to non-destructive and spatially-resolved features, THz-TDS allows a full determination of graphene electronic properties such as sheet conductivity, carrier density, carrier scattering time and

carrier mobility (Figure 4h, 4i and Figure S20b–f), which has previously been shown to agree well with transport measurements.^[37] The drift mobility of monolayer graphene was found to have an average value of $6903 \text{ cm}^2\text{V}^{-1}\text{s}^{-1}$ with a standard deviation of $1420 \text{ cm}^2/\text{Vs}$ (Figure 4i). The measured level of uniformity and average mobility of the monolayer graphene is high compared to that of the corresponding graphene film containing multi-layered regions, and also high compared to previously reported CVD grown graphene samples including single-crystal graphene film determined by THz-TDS technique (Table S2), indicating high electronic quality of our pure and continuous monolayer graphene.

We further performed several techniques for revealing the crystallinity of graphene samples over a large length scale. For example, we found that all partially-covered graphene domains grown on Cu(111) before their merging show a good alignment in our experimental conditions (Figure S21). Note that the shapes of graphene domains are dependent on growth conditions and Cu(111) substrate, variously-shaped graphene domains deviated from ideal hexagonal shapes were observed in our growth condition. The good alignment of graphene domains leads to a large-scale single-crystal graphene film. As-grown monolayer graphene films were also further etched at the growth temperature without the presence of CH_4 , and the results showed that etched holes are also well-aligned over the whole area of graphene film (Figure S22–S24), indicating its single-crystal nature.^[38–40] In addition, low-energy electron diffraction (LEED) technique was conducted on as-grown monolayer graphene film on Cu(111) (Figure S25). The results show two distinguishable sets of six-fold diffraction patterns that are close to each other, in which the pattern far away from the center is attributed to graphene lattice (graphene lattice 2.46 \AA , and the underlying Cu lattice 2.56 \AA ^[41]), and the same orientation of two diffraction patterns for two locations separated by 2 mm provides an additional evidence of single-crystal graphene. Finally, the observed coalesced graphene grains with rounded concave corners (Figure S26) indicate their seamless coalescence,^[3, 42] and direct

TEM selected area electron diffraction (SAED) measurement (Figure S27) further confirms the absence of GBs in coalesced graphene islands.

The changes from various states of multi-layered graphene to a single state of uniform monolayer graphene are intriguing. A flow diagram of the whole process consisting of the first graphene growth and the second etching process is shown in **Figure 5a**. Generally, compared to the upper layer, less C supplies are provided for lower graphene layers due to the limited diffusion of C precursors within the lower confined space, possibly resulting in a layer spatial-order-dependent etching, i.e., the upper layer is corresponding to the lower etching rate. Many strong evidences were found to support the “bottom-up-etching” in our experiments. For instance, Figure 5b–d and Figure S28 show typical SEM and optical images of graphene samples at the second etching stage transferred onto 300 nm SiO₂/Si substrates. While graphene monolayer (G₁) remains a continuous film, the underlying graphene layers (G₂ or G₃) appear the loss of their natural integrity or contain holes with well-defined hexagonal shapes, which is associated with the etching of these lower graphene multi-layers. Etching rates for different layers can be clearly derived by comparing different etching area in local imaging of samples. Raman spectra of labelled area (Figure 5d) are indeed consistent with graphene layer numbers using direct optical images (Figure 5e). Further Raman mappings of these samples’ G and 2D peak intensities not only show the contrast of different layer numbers that are consistent with the corresponding optical images, but also reveal the typical layer-stacking information (Figure 5f–h and 5i–k). Compared with 2D peak intensity of monolayer graphene, 2D peak intensities of bilayer graphene show higher and lower intensity at different regions. These observations reflect a different coupling strength of bilayer with different stacking order.^[43,44] In the case of two layers with 0° orientation (AB or Bernal stacking), the intensity of 2D peak for two layers is significantly reduced due to a strong coupling between two layers. In contrast, for 30° orientations, 2D peak intensity of bilayer is usually higher than that of monolayer graphene.^[45] These behaviors were generally found in our samples (Figure S29–S31). Finally, in

This article is protected by copyright. All rights reserved.

practice, as the growth and etching of graphene are sensitive to experimental conditions such as temperature, the flow ratio of Ar to H₂ and trace amount of H₂O or O₂,^[46] the flow rate of CH₄ and in-situ etching duration are experimentally determined. A set of non-uniform multi-layered graphene films grown at different conditions can be converted to uniform monolayer state under tunable growth-etching conditions.

2.4 DFT and phase field simulations for the formation of uniform graphene monolayer

To understand the growth and selective etching of graphene in our experiments, extensive first-principles DFT calculations and phase field simulations were performed. It has been found that CH₄ cannot stay on Cu(111) surface under a typical graphene CVD temperature (1300 K) due to its small binding energy (0.05 eV) on Cu surface.^[47] Our calculations showed that dissociation of H₂ molecules into H atoms is energetically favorable on Cu(111) surface (Figure S32). Therefore, hydrocarbon radicals and H atoms on Cu surface are responsible for the growth and etching of graphene during CVD, as schematically shown in **Figure 6a**. We then calculated the formation energies of CH_i (i = 0, 1, 2 and 3) on a bare Cu(111) surface and at the interface between graphene and Cu(111), respectively (Please refer to SI for calculation details). Under a relatively high chemical potential of H, such as H atom on Cu(111), the formation energy of CH₃ on bare Cu(111) surface is lowest, suggesting that CH₃ are dominant among all the carbon radicals considered (Figure 6b). With the decrease of the chemical potential of H, the formation energy of C atoms (or carbon dimers C₂, which were found to be even more stable than C monomers^[47,48]) on bare Cu(111) surface will become the most stable and the dominant species (Figure S33). Our results are consistent with previous studies.^[47,48] Importantly, it can be seen that all carbon radicals at the interface between graphene and Cu(111) show higher formation energies than those on bare Cu(111) surface, leading to their lower concentrations and thus a slower growth rate of graphene multi-layers beneath the graphene top-layer. The diffusion of H atoms, C₂ and CH and CH₃ radicals, which were found to be dominant under

a high H_2 partial pressure,^[47,48] from bare Cu(111) surface to the graphene-Cu interface were also explored. As shown in Figure 6c–e and Figure S34–S37, the diffusion of H atoms to the graphene-Cu interface is much easier than C_2 , CH and CH_3 , which further proves the more difficult growth and much easier etching of graphene multi-layers than the top-layer. Consequently, a continuous graphene monolayer with sparsely distributed multi-layers will be formed during growth.

After the full coverage of the top graphene layer, we propose that selective etching of the multi-layers can be realized by properly decreasing the supply of CH_4 to keep the top-layer and multi-layers of graphene under near-equilibrium and carbon-deficient environments, respectively. Because the synthesis of graphene via CH_4 follows $CH_4 \rightleftharpoons CH_3 \rightleftharpoons CH_2 \rightleftharpoons \dots \rightleftharpoons$ Graphene and CH_4 cannot stay on Cu(111) surface under a high growth temperature, we then compared the chemical potential difference between CH_3 radicals ($\mu_{CH_3}(\rho_{CH_3}, T)$), H atoms ($\mu_H(\rho_H, T)$), and graphene top-layer ($\mu_G(T)$) on Cu(111) surface:

$$\Delta G = \mu_{CH_3}(\rho_{CH_3}, T) - 3\mu_H(\rho_H, T) - \mu_G(T) \quad (2)$$

where ρ_{CH_3} and ρ_H are the concentrations of CH_3 radicals and H atoms on the Cu(111) surface, respectively, which can be estimated from the partial pressures of CH_4 (P_{CH_4}) and H_2 (P_{H_2}) at a temperature of T based on a simplified adsorption-dissociation-desorption model (Please refer to SI for details.). Figure 6f shows the predicted critical P_{CH_4} and P_{H_2} (marked by black line) for at which $\Delta G = 0$ is satisfied under 1300 K. Growth and etching of the graphene top-layer are expected under conditions far above and below this predicted boundary, respectively, while a near-equilibrium environment for graphene synthesis can be achieved under conditions close to this boundary. This prediction is in good agreement with our experiments, where the square dot in Figure 6f denotes the typical partial pressures of CH_4 and H_2 used for graphene growth at 1348 K. By slightly decreasing the supply of CH_4 and keep the supply of H_2 unchanged (circular dot in Figure 6f), the concentrations of

CH_i radicals beneath the graphene top-layer were reduced and therefore etching of the multi-layers can be achieved, while near equilibrium of the graphene top-layer can still be maintained.

Phase field theory simulations were performed to demonstrate the selective etching process (Please refer to SI for details.). Figure 6g schematically shows an atomic model of an as-grown graphene monolayer with an extra layer beneath it, both of which were nucleated near an impurity particle, as observed in our experiments. At the initial selective etching stage, a hole in the two graphene layers at the nucleation site will be formed (first panels in Figure 6h and 6i, respectively). Because the diffusion of H atoms into the interface between the top-layer graphene and Cu surface is much easier than CH_3 , the relative concentration ratio of H atoms to CH_3 radicals at the graphene-Cu interface is much higher than that on the bare Cu surface, and thus etching of the bottom-layer is much faster than that of the top-layer. With the etching continued, concentration of carbon radicals at the graphene-Cu interface will increase and these carbon radicals will diffuse out to the bare Cu surface near the nucleation center, which subsequently stops the etching and even leads to re-growth of the graphene top-layer (Figure 6h–j and Figure S38), and a hexagonal hole will develop only in the bottom-layer. It should be noted that carbon radicals etched from the graphene bottom-layers cannot directly desorb from the substrate surface. Instead, they can only diffuse away to other areas of the graphene-Cu interface or to the air through defects of the graphene top-layer. Therefore, the evolution of the outer circumference of a graphene bottom-layer during etching is not the same as that of hexagonal top-layer graphene islands,^[49] where the six vertices are quickly etched away and twelve tilt edges appear to dominate the circumference. For the etching of a graphene bottom-layer, the faster etching of vertices than edges leads to higher concentrations of carbon radicals near to the vertices than edges (Figure 6j), which in-turn lowers down the etching rate of vertices. Consequently, the shape of the outer circumference of the bottom-layer will not change significantly during etching (Figure 6i, Figure S39 and S40), which is also consistent with our experimental observations (Figure S20).

This article is protected by copyright. All rights reserved.

3. Conclusion

In summary, this work develops a cyclic “electrochemical polishing and thermal annealing” approach that allows the production of large-scale Cu(111) with almost 100% yield and wide applications. Electrochemical polishing and cyclic operation are particularly effective for reducing energy barriers of GB migration and pinning. Using key evidences of GB migration, flattening and merging, we develop a framework that allows the understanding of the complex conversion. We further demonstrate a global “bottom-up-etching” method that is capable of etching away multi-layered graphene, leading to a realization of producing a uniform monolayer graphene film on Cu(111) surface. These approaches and the corresponding understanding of mechanism are key to the realization of high-quality single-crystal substrate and the controlled growth of graphene or other 2D materials.

4. Experimental Section/Methods

Synthesis of single-crystal Cu(111) foils: Single-crystal Cu(111) foils were prepared by a cyclic electrochemical polishing and high temperature annealing process as follows. First, commercial Cu foils were electrochemically polished. The solution consists of deionized water, ethanol, phosphoric acid, isopropanol and carbamide with the proportion of 10 : 5 : 5 : 1 : 0.16. Cu foil serves as the anode with a voltage of about 3–5 V, and a typical process takes a few minutes. After polishing, Cu foils were thermally annealed at a temperature close to the melting point of Cu with a flow of H₂ or a mixture of Ar (200 sccm) and H₂ (50) for about 0.5–1h. 2–4 cycles of this process lead to single-crystal Cu(111) foils.

Synthesis and transfer of multi-layer and uniform monolayer graphene films: The experiments were performed in a CVD system with a 2-inch quartz tube. Briefly, as-prepared single-crystal Cu(111) foils were placed on a quartz tube. When the temperature was raised to be 1075 °C with a flow of 250

This article is protected by copyright. All rights reserved.

Accepted Article

sccm Ar and 20 sccm H₂, 4–8 sccm methane diluted in argon (0.5 % in Ar) was introduced into the tube for about 1h, resulting in a multi-layer graphene film. For monolayer graphene growth, the flow rate of CH₄ was reduced to a small value typically in the range of 0.2–0.5 sccm for selectively etching multi-layer graphene, and the duration is about 2.5–3.5 h. In addition, for carbon isotope ¹²CH₄ (99.9% purity) was first used to grow graphene islands. and then switched off followed by the introduction of ¹³CH₄ (99% purity) to the growth system. Briefly, an extra valve in ¹²CH₄ gas path was installed for controlling the diffusion of ¹²CH₄ to main gas path. Before the dosing of ¹³CH₄, a flow of 500 sccm Ar was introduced to purge the system for 1 min after stopping the dosing of ¹²CH₄. All the experiments were performed at ambient pressure. As-grown graphene samples were transferred onto 300 nm SiO₂/Si substrates for Raman tests and oxygen plasma treatment. Finally, the flow of CH₄ was switched off, and the system was quickly cooled down to room temperature. The transfer of graphene samples on Cu is conducted by using traditional wet transfer methods. Briefly, the PMMA solution was spin-coated on the graphene sample on the surface of the Cu foil at a speed of 3000 r/min, and baked at 120 °C for 10 minutes. The PMMA/graphene/Cu samples are then placed into a saturated FeCl₃ solution. After the Cu foils are completely etched, the PMMA/graphene sample layers are washed with diluted HCl and deionized water several times, and then the samples are transferred to a 300 nm SiO₂/Si substrate.

Terahertz time-domain reflection spectroscopy: THz-TDS measurements were conducted using a commercially available fiber-coupled spectrometer (Teraflash system). The Teraflash system uses a robust, femtosecond laser system with wavelength centered at 1560 nm and a photoconductive antenna with high-mobility InAlAs/InGaAs multilayer heterostructure to generate picosecond electromagnetic terahertz pulse. The detector coherent to the emitter is based on the photoconductive with an LT-grown Beryllium doped InAlAs/InGaAs multilayer heterostructure. One piece of high-resistivity silicon wafer ($\rho > 10000 \Omega cm$) is used as a beam splitter, which allows terahertz pulse normal incident and reflected on the sample. Spatial THz-TDS maps with 250 μm step

size were acquired by raster scanning the samples at normal incidence in the focal plane of the THz beam and the THz spot size is 1 mm at 1 THz. The frequency-dependent sheet conductivity of graphene was extracted from the ratio of THz radiation passing through graphene-covered sample regions $E_s(\omega)$ and THz radiation passing through a substrate reference area with no graphene

$$E_r(\omega): r = \frac{E_s(\omega)}{E_r(\omega)} = \left| \frac{1-n_{sub}-Z_0\sigma(\omega)}{1+n_{sub}+Z_0\sigma(\omega)} \frac{1+n_{sub}}{1-n_{sub}} \right|, \text{ where } n_{sub} \text{ is the refractive index of substrate and } Z_0 \text{ is}$$

the free space impedance. THz-TDS sheet conductivity maps show the spatially averaged sheet conductivity in the 0.4–1.4 THz range. The DC conductivity σ_{DC} and scattering time τ can be extracted from THz-TDS measurements of graphene by fitting the frequency-dependent sheet conductivity of graphene to the Drude-model, $\sigma(\omega) = \sigma_{dc}/(1 - i\omega\tau)$, where $\sigma(\omega)$ is the frequency-dependent sheet conductivity. The carrier density n and mobility μ of graphene can subsequently be

$$\text{calculated from } n = \frac{\pi\hbar^2\sigma_{DC}^2}{e^4v_F^2\tau^2} \text{ and } \mu = \sigma_{DC}/ne, \text{ where } v_F \text{ is the Fermi velocity set to } 10^6 \text{ m/s.}$$

Characterizations: Samples were characterized by optical microscope (Olympus DX51, Olympus), scanning electron microscopy (Hitachi S-4800), Raman spectroscopy with an excitation wavelength 532 nm (Renishaw inVia, Renishaw), Powder X-ray diffraction (PANalytical Empyrean diffractometer using Cu radiation) and XPS (ESCALAB250XI). AFM images were taken with Veeco Nanoscope IIIa, tapping mode. TEM was conducted by JEOL 2010F. LEED were performed under ultrahigh vacuum of 1×10^{-10} Torr (Elmitec LEEM-III system). EBSD data were obtained with ULVAC-PHI 710 under the voltage of 15 kV and the current of 10 nA, and the probe model is EDAX OIM 6.0. X-ray fluorescence analyses (XRF) of samples were carried out on a PANalytical Zetium spectrometer. The films were analyzed by wavelength-dispersive XRF, and the data were analyzed by Omnic method. The SIMS analysis was performed with a ToF-SIMS 5 instrument (ION-ToF GmbH, Münster, Germany) equipped with a 30 keV Bi^{3+} primary ion gun and a 10 keV Ar sputter gun. An electron flood gun was used for charge neutralization. The theoretical calculations were carried out on TianHe-1(A) at National Supercomputer Center at Tianjin.

Supporting Information

Supporting Information is available from the Wiley Online Library or from the author.

Acknowledgements

This work was supported by the National Basic Research Program of China (2016YFA0200101), the National Natural Science Foundation of China (21633012 and 61890940), Chinese Academy of Sciences and the Strategic Priority Research Program of the Chinese Academy of Sciences (XDB30000000), and the CAS Key Research Program of Frontier Sciences (QYZDY-SSW-SLH029). The authors thank Prof. Chengmin Shen for the help of LEED measurements of samples. The theoretical calculations were carried out on TianHe-1(A) at National Supercomputer Center at Tianjin.

Received: ((will be filled in by the editorial staff))

Revised: ((will be filled in by the editorial staff))

Published online: ((will be filled in by the editorial staff))

References

- [1] W. Yao, B. Wu, Y. Liu, *ACS Nano*, **2020**, *14*, 9320.
- [2] J. Zhang, L. Lin, K. Jia, L. Sun, H. Peng, Z. Liu, *Adv. Mater.* **2020**, *32*, e1903266.
- [3] V. L. Nguyen, B. G. Shin, D. L. Duong, S. T. Kim, D. Perello, Y. J. Lim, Q. H. Yuan, F. Ding, H. Y. Jeong, H. S. Shin, S. M. Lee, S. H. Chae, Q. A. Vu, S. H. Lee, Y. H. Lee, *Adv. Mater.* **2015**, *27*, 1376.
- [4] J. Dong, L. Zhang, X. Dai, F. Ding, *Nat. Commun.* **2020**, *11*, 5862.
- [5] L. Wang, X. Xu, L. Zhang, R. Qiao, M. Wu, Z. Wang, S. Zhang, J. Liang, Z. Zhang, Z. Zhang, W. Chen, X. Xie, J. Zong, Y. Shan, Y. Guo, M. Willinger, H. Wu, Q. Li, W. Wang, P. Gao, S. Wu, Y. Zhang, Y. Jiang, D. Yu, E. Wang, X. Bai, Z. -J. Wang, F. Ding, K. Liu, *Nature* **2019**, *570*, 91.
- [6] B. Deng, Z. Pang, S. Chen, X. Li, C. Meng, J. Li, M. Liu, J. Wu, Y. Qi, W. Dang, H. Yang, Y. Zhang, J. Zhang, N. Kang, H. Xu, Q. Fu, X. Qiu, P. Gao, Y. Wei, Z. Liu, H. Peng, *ACS Nano* **2017**, *11*, 12337.
- [7] T.-A. Chen, C.-P. Chuu, C.-C. Tseng, C.-K. Wen, H.-S. Philip Wong, S. Pan, R. Li, T.-A. Chao, W.-C.

This article is protected by copyright. All rights reserved.

- Chueh, Y. Zhang, Q. Fu, B. I. Yakobson, W.-H. Chang, L.-J. Li, *Nature* **2020**, *579*, 219.
- [8] L. Brown, E. B. Lochocki, J. Avila, C. J. Kim, Y. Ogawa, R. W. Havener, D. K. Kim, E. J. Monkman, D. E. Shai, H. I. Wei, M. P. Levendorf, M. Asensio, K. M. Shen, J. Park, *Nano Lett.* 2014, *14*, 5706.
- [9] H. D. Phan, J. Jung, Y. Kim, V. N. Huynh, C. Lee, *Nanoscale* 2016, *8*, 13781.
- [10] X. Xu, Z. Zhang, J. Dong, D. Yi, J. Niu, M. Wu, L. Lin, R. Yin, M. Li, J. Zhou, S. Wang, J. Sun, X. Duan, P. Gao, Y. Jiang, X. Wu, H. Peng, R. S. Ruoff, Z. Liu, D. Yu, E. Wang, F. Ding, K. Liu, *Sci. Bull.* **2017**, *62*, 1074.
- [11] B. Deng, Z. Xin, R. Xue, S. Zhang, X. Xu, J. Gao, J. Tang, Y. Qi, Y. Wang, Y. Zhao, L. Sun, H. Wang, K. Liu, M. H. Rummeli, L.-T. Weng, Z. Luo, L. Tong, X. Zhang, C. Xie, Z. Liu, H. Peng, *Sci. Bull.* **2019**, *64*, 659.
- [12] S. Jin, M. Huang, Y. Kwon, L. Zhang, B.-W. Li, S. Oh, J. Dong, D. Luo, M. Biswal, B. V. Cunniff, P. V. Bakharev, I. Moon, W. J. Yoo, D. C. Camacho-Mojica, Y.-J. Kim, S. H. Lee, B. Wang, W. K. Seong, M. Saxena, F. Ding, H. -J. Shin, R. S. Ruoff, *Science* **2018**, *362*, 1021.
- [13] M. Wu, Z. Zhang, X. Xu, Z. Zhang, Y. Duan, J. Dong, R. Qiao, S. You, L. Wang, J. Qi, D. Zou, N. Shang, Y. Yang, H. Li, L. Zhu, J. Sun, H. Yu, P. Gao, X. Bai, Y. Jiang, Z. -J. Wang, F. Ding, D. Yu, E. Wang, K. Liu, *Nature* **2020**, *581*, 406.
- [14] A. T. Murdock, A. Koos, T. Ben Britton, L. Houben, T. Batten, T. Zhang, A. J. Wilkinson, R. E. Dunin-Borkowski, C. E. Lekka, N. Grobert, *ACS Nano* **2013**, *7*, 1351.
- [15] J. Li, J. Zhuang, C. Shen, Y. Tian, Y. Que, R. Ma, J. Pan, Y. Zhang, Y. Wang, S. Du, F. Ding, H. -J. Gao, *Nano Res.* **2016**, *9*, 2803.
- [16] J. D. Wood, S. W. Schmucker, A. S. Lyons, E. Pop, J. W. Lyding, *Nano Lett.* **2011**, *11*, 4547.
- [17] G. H. Han, F. Gunes, J. J. Bae, E. S. Kim, S. J. Chae, H.-J. Shin, J.-Y. Choi, D. Pribat, Y. H. Lee, *Nano Lett.* **2011**, *11*, 4144.
- [18] B. Deng, Y. Hou, Y. Liu, T. Khodkov, S. Goossens, J. Tang, Y. Wang, R. Yan, Y. Du, F. H. L. Koppens, X. Wei, Z. Zhang, Z. Liu, H. Peng, *Nano Lett* **2020**, *20*, 6798.

- [19] D. Luo, M. Wang, Y. Li, C. Kim, K. M. Yu, Y. Kim, H. Han, M. Biswal, M. Huang, Y. Kwon, M. Goo, D. C. Camacho-Mojica, H. Shi, W. J. Yoo, M. S. Altman, H. J. Shin, R. S. Ruoff, *Adv. Mater.* **2019**, *31*, e1903615.
- [20] Y. Ogawa, B. Hu, C. M. Orofeo, M. Tsuji, K. Ikeda, S. Mizuno, H. Hibino, H. Ago. *J. Phys. Chem. Lett.* **2012**, *3*, 219.
- [21] Y. Li, L. Sun, Z. Chang, H. Liu, Y. Wang, Y. Liang, B. Chen, Q. Ding, Z. Zhao, R. Wang, Y. Wei, H. Peng, L. Lin, Z. Liu, *Adv. Mater.* **2020**, *32*, e2002034.
- [22] Z. Luo, Y. Lu, D. W. Singer, M. E. Berck, L. A. Somers, B. R. Goldsmith, A. T. C. Johnson, *Chem. Mater.* **2011**, *23*, 1441.
- [23] Z. Zhang, X. Xu, Z. Zhang, M. Wu, J. Wang, C. Liu, N. Shang, J. Wang, P. Gao, D. Yu, E. Wang, K. Liu, *Adv. Mater. Interfaces* **2018**, *5*, 1800377.
- [24] J. Ciulik, E. M. Taleff, *Scr. Mater.* **2009**, *61*, 895.
- [25] T. Kusama, T. Omori, T. Saito, S. Kise, T. Tanaka, Y. Araki, R. Kainuma, *Nat. Commun.* **2017**, *8*, 354.
- [26] S. L. Thomas, K. Chen, J. Han, P. K. Purohit, D. J. Srolovitz, *Nat. Commun.* **2017**, *8*, 1764.
- [27] C. Braun, J. M. Dake, C. E. Krill III, R. Birringer, *Sci. Rep.* **2018**, *8*, 1592.
- [28] P. A. Manohar, M. Ferry, T. Chandra, *ISIJ Int.* **1998**, *38*, 913.
- [29] N. Lua, J. Kangb, N. Senabulyac, R. Keinana, N. Guenincha, A. J. Shahania, *Acta Mater.* **2020**, *195*, 1.
- [30] E. A. Holm, S. M. Foiles, *Science* **2010**, *328*, 1138.
- [31] W. Fang, A. L. Hsu, Y. Song, J. Kong, *Nanoscale* **2015**, *7*, 20335.
- [32] M. Huang, R. S. Ruoff, *Acc. Chem. Res.* **2020**, *53*, 800.
- [33] B. Wu, D. Geng, Y. Guo, L. Huang, Y. Xue, J. Zheng, J. Chen, G. Yu, Y. Liu, L. Jiang, W. Hu, *Adv. Mater.* **2011**, *23*, 3522.
- [34] Q. Li, H. Chou, J.-H. Zhong, J.-Y. Liu, A. Dolocan, J. Zhang, Y. Zhou, R. S. Ruoff, S. Chen, W. Cai,

Nano Lett. **2013**, *13*, 486.

- [35] W. Fang, A. L. Hsu, R. Caudillo, Y. Song, A. Glen Birdwell, E. Zakar, M. Kalbac, M. Dubey, T. Palacios, M. S. Dresselhaus, P. T. Araujo, J. Kong, *Nano Lett.* **2013**, *13*, 1541.
- [36] X. Zhang, L. Wang, John. Xin, B. I. Yakobson, F. Ding, *J. Am. Chem. Soc.* **2014**, *136*, 3040.
- [37] P. R. Whelan, B. Zhou, O. Bezencenet, A. Shivayogimath, N. Mishra, Q. Shen, B. S. Jessen, I. Pasternak, D. M. A. Mackenzie, J. Ji, S. Cunzhi, P. Seneor, B. Dlubak, B. Luo, F. Østerberg, D. Huang, H. Shi, D. Luo, M. Wang, R. S. Ruoff, B. Conran, C. McAleese, C. Huyghebaert, S. Brems,; T. Booth, I. Napal, W. Strupinskii, D. H. Petersen, S. Forti, C. Coletti, A. Jouvray, K. B. K. Teo, A. Centeno, A. Zurutuza,; P. Legagneux, P. U. Jepsen, P. Boggild, *2D Mater.* **2021**, *8*, 022003.
- [38] Q. Li, H. Chou, J.-H. Zhong, J.-Y. Liu, A. Dolocan, J. Zhang, Y. Zhou, R. S. Ruoff, S. Chen, W. Cai, *ACS Nano* **2015**, *9*, 5792.
- [39] I. V. Vlassiuk, Y. Stehle, P. R. Pudasaini, R. R. Unocic, P. D. Rack, A. P. Baddorf, I. N. Ivanov, N. V. Lavrik, F. List, N. Gupta, K. V. Bets, B. I. Yakobson, S. N. Smirnov, *Nat. Mater.* **2018**, *17*, 318.
- [40] X. Chen, H. Yang, B. Wu, L. Wang, Q. Fu, Y. Liu, *Adv. Mater.* **2019**, *31*, e1805582.
- [41] L. Gao, J. R. Guest, N. P. Guisinger, *Nano Lett.* **2010**, *10*, 3512.
- [42] Z. J. Wang, J. Dong, L. Li, G. Dong, Y. Cui, Y. Yang, W. Wei, R. Blume, Q. Li, L. Wang, X. Xu, K. Liu, C. Barroo, J. W. M. Frenken, Q. Fu, X. Bao, R. Schlögl, F. Ding, M. G. Willinger, *ACS Nano* **2020**, *14*, 1902.
- [43] D. Graf, F. Molitor, K. Ensslin, C. Stampfer, A. Jungen, C. Hierold, L. Wirtz, *Nano Lett.* **2007**, *7*, 238.
- [44] K. Kim, S. Coh, L. Z. Tan, W. Regan, J. M. Yuk, E. Chatterjee, M. F. Crommie, M. L. Cohen, S. G. Louie, A. Zettl, *Phys. Rev. Lett.* **2012**, *108*, 246103.
- [45] Y. Li, B. Wu, W. Guo, L. Wang, J. Li, Y. Liu, *Nanotechnology* **2017**, *28*, 265101.
- [46] W. Guo, B. Wu, S. Wang, Y. Liu, *ACS Nano* **2018**, *12*, 1778.
- [47] H. Shu, X. M. Tao, F. Ding, *Nanoscale* **2015**, *7*, 1627.

This article is protected by copyright. All rights reserved.

[48] P. Li, Z. Li, J. Yang, *J. Phys. Chem. C* **2017**, *121*, 25949.

[49] T. Maa, W. Ren, X. Zhang, Z. Liu, Y. Gao, L. C. Yina, X. L. Maa, F. Ding, H. M. Cheng, *Proc. Natl. Acad. Sci. USA* **2013**, *110*, 20386.

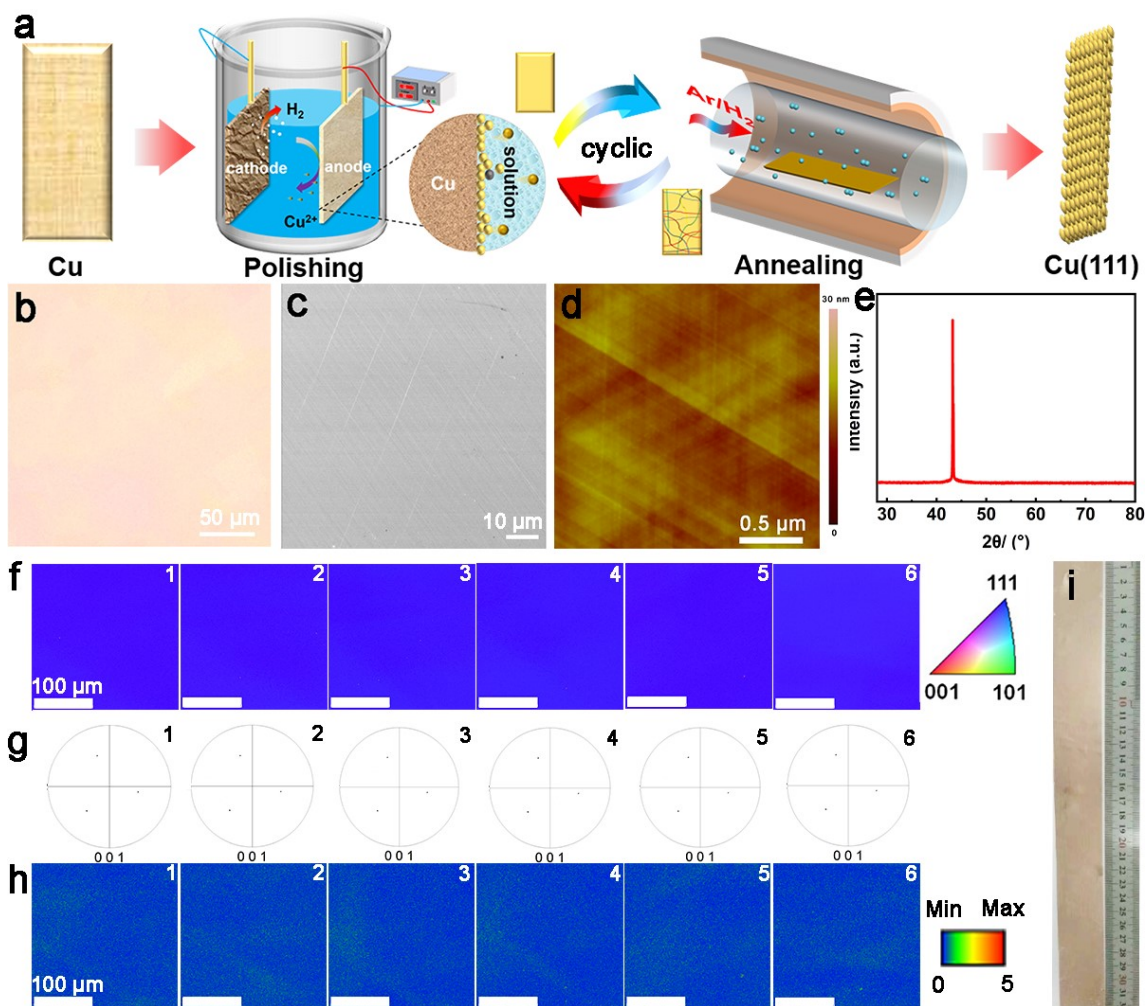


Figure 1. The preparation process and characterizations of single-crystal Cu(111) foils. (a) Schematic illustration for the preparation of single-crystal Cu(111) by cyclic electrochemical polishing and thermal annealing. (b–d) Typical optical, SEM and AFM images of as-prepared Cu(111) surface, respectively. (e) Typical XRD data of Cu(111) foil with a single and sharp peak located at 43.3° . (f–h) Typical EBSD inverse pole figure (IPF) mappings in the normal direction (f), (001) pole figures (g) and KAM maps (h) of six different regions separated by about 1cm on Cu(111) surface. i) Photograph of Cu(111) foil with a size of $4 \times 32 \text{ cm}^2$.

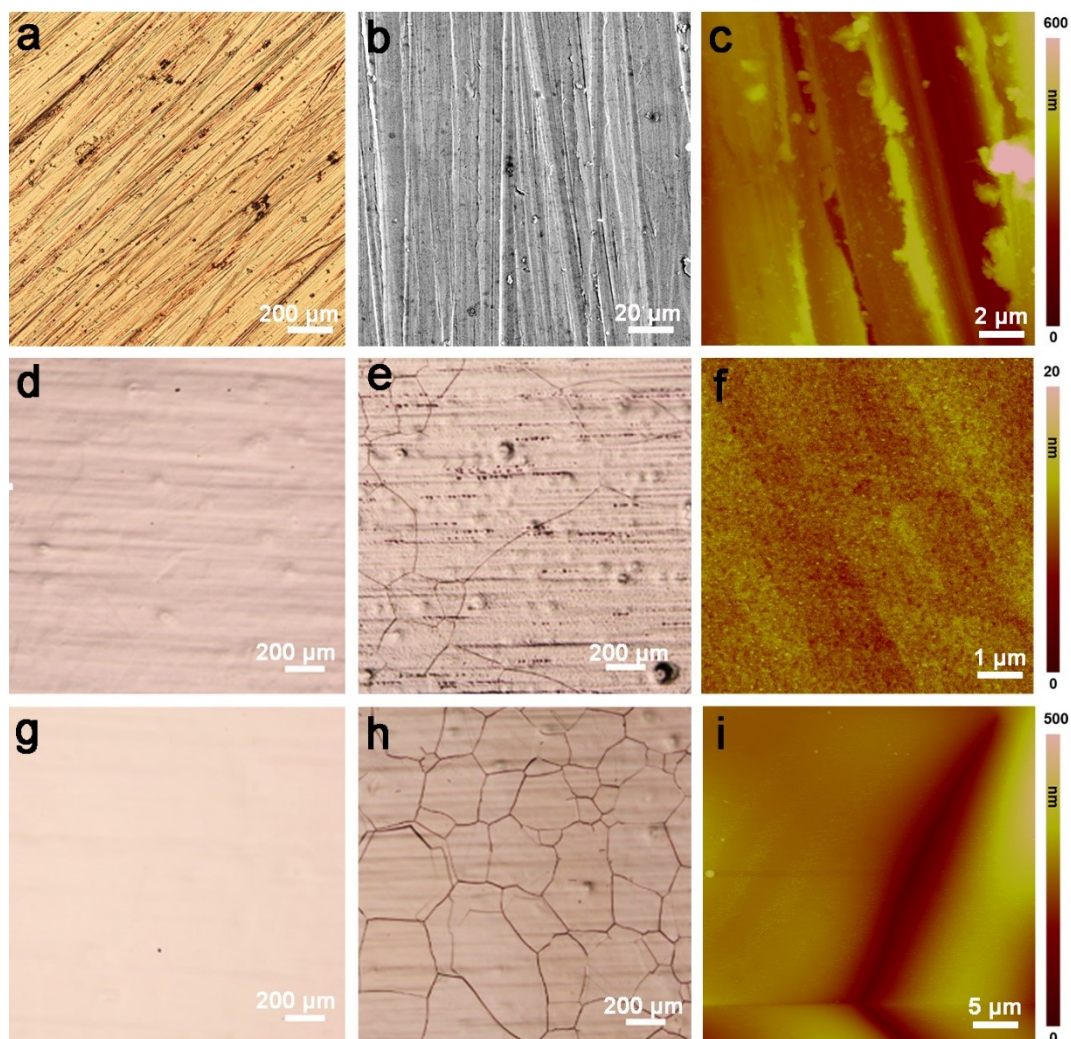


Figure 2. Characterizations of Cu surface at different stages of electrochemical polishing and annealing. (a–c) Optical, SEM and AFM images of commercial polycrystalline Cu, respectively. (d, e) Optical and AFM images of Cu surface after the first polishing process, respectively. (f) Optical image of Cu surface after the first annealing. (g) Optical image of Cu surface after the second polishing. (h) Optical image of Cu surface after the second annealing. (i) AFM image of typical GB grooves.

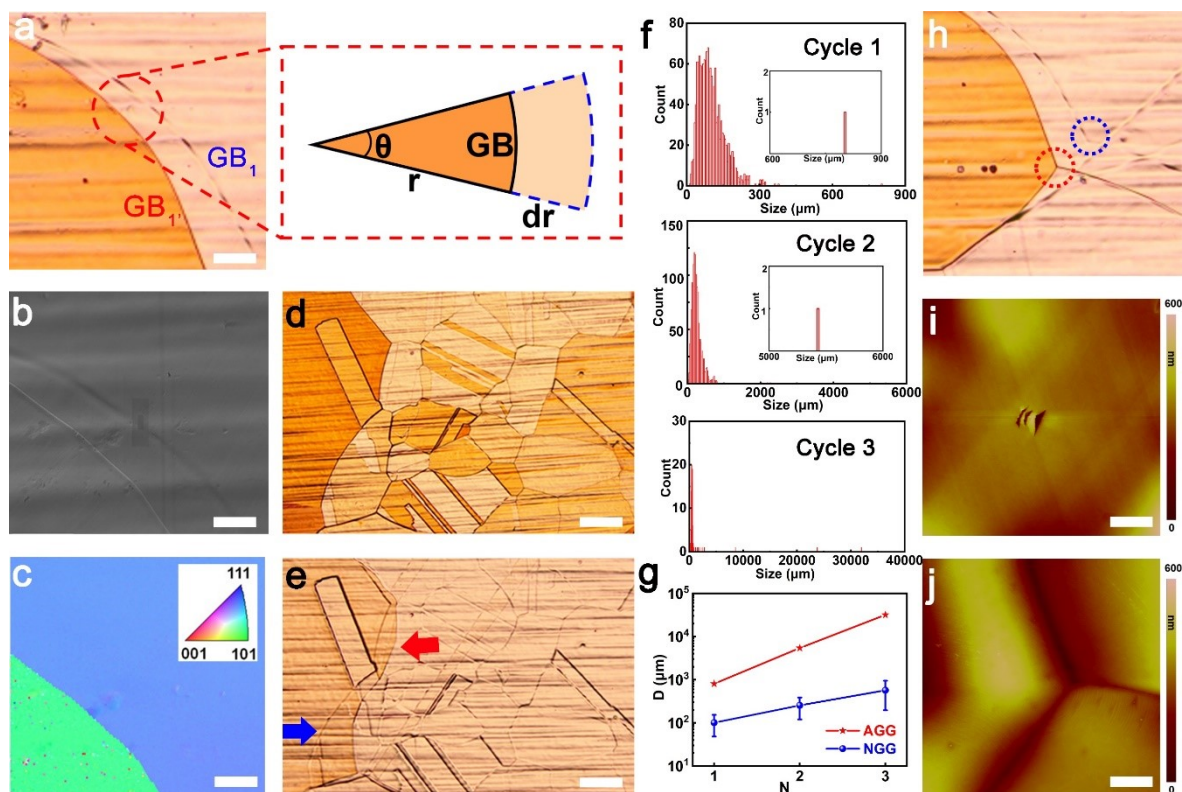


Figure 3. Characterization of GBs migration. (a–c) Optical, SEM and EBSD characterizations of the same location on Cu involving a GB movement, respectively. The right schematic of (a) illustrates the profiles of GBs before and after migration. The line marked with GB1 indicates the original GB and the line marked with GB₁ indicates the newly-formed GB after migration toward the center of curvature. The scale bars are 50 μm, 60 μm and 60 μm, respectively. (d) Optical image of the Cu region after the second polishing and annealing treatment. (e) Optical image of Cu region after the third polishing and annealing treatment, showing abnormal growth of large Cu(111) grain and a behavior of GB movement towards Cu(111) region, indicating the initial (blue arrow) and newly-formed (red arrow) GBs. The scale bars are 200 μm. (f) Histograms of Cu grain sizes with the treatment of different cycles. (g) Plots of average Cu grain sizes in NGG and AGG as a function of cycle numbers. (h) Optical image of a location involving the movement of interconnected GBs. (i, j) AFM images of blue and red areas labelled in h, respectively, showing that the grooves in the original GB areas were not found after GB migration, and the heights of newly-formed GB grooves are in the range of 100–400 nm. The scale bars are 5 μm and 10 μm, respectively.

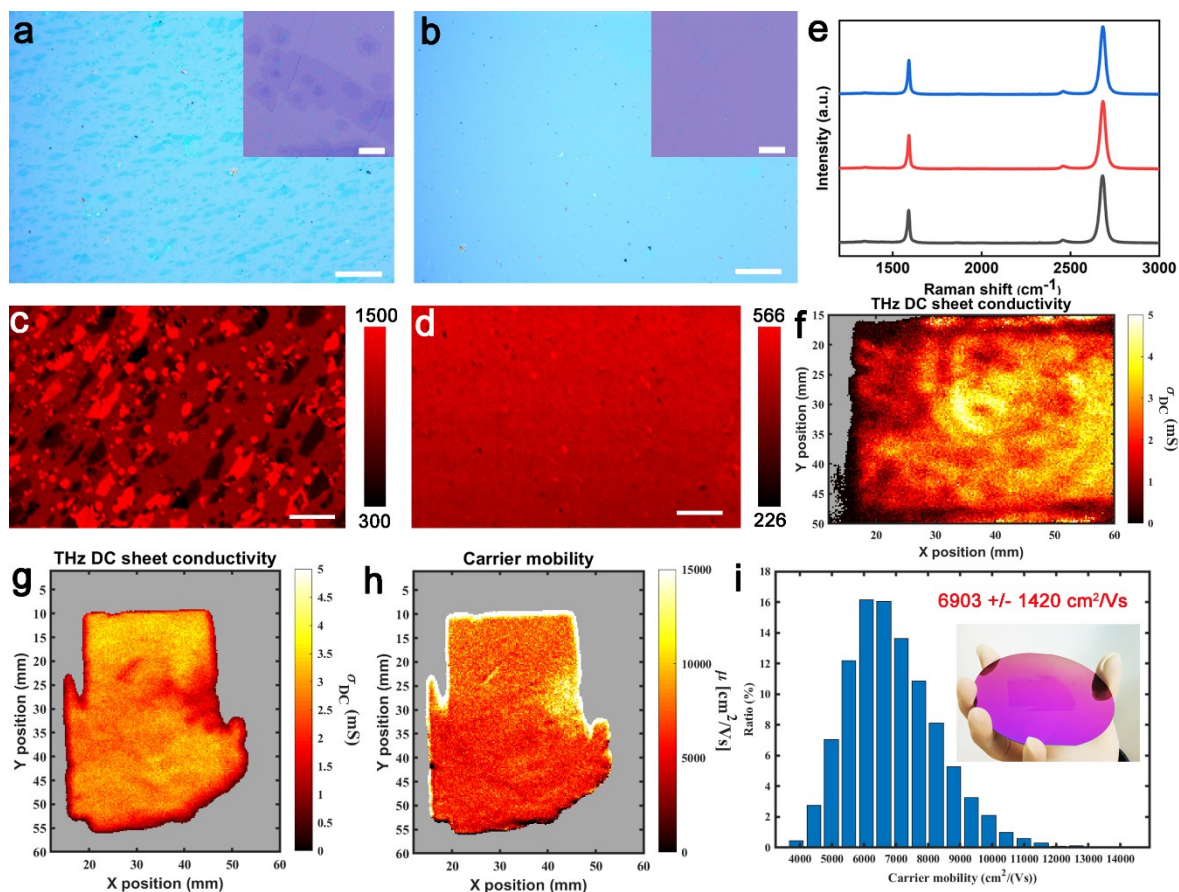


Figure 4. The synthesis of uniform monolayer graphene films on Cu(111) surface and THz-TDS characterization of graphene electronic properties. (a, b) Optical images of multi-layered graphene and uniform monolayer graphene films transferred onto 300 nm SiO_2/Si substrates, respectively. The scale bars in a and b are 100 μm and 200 μm , respectively. Inset: The corresponding close-up optical images of a and b. The scale bars are 10 μm . (c, d) The comparison of large-scale Raman mappings of 2D peak intensities for multi-layer and monolayer graphene films, respectively. The scale bars are 50 μm . (e) Typical Raman spectra of monolayer graphene films measured at randomly different locations. (f) THz-TDS sheet conductivity map of graphene film with multi-layered portion transferred onto a 300 nm SiO_2/Si wafer. (g, h) THz-TDS sheet conductivity and carrier mobility maps of monolayer graphene film transferred onto a 300 nm SiO_2/Si wafer, respectively. (i) Carrier mobility histogram. Inset: Photograph of a monolayer graphene film transferred onto a 300 nm SiO_2/Si wafer for THz-TDS measurement.

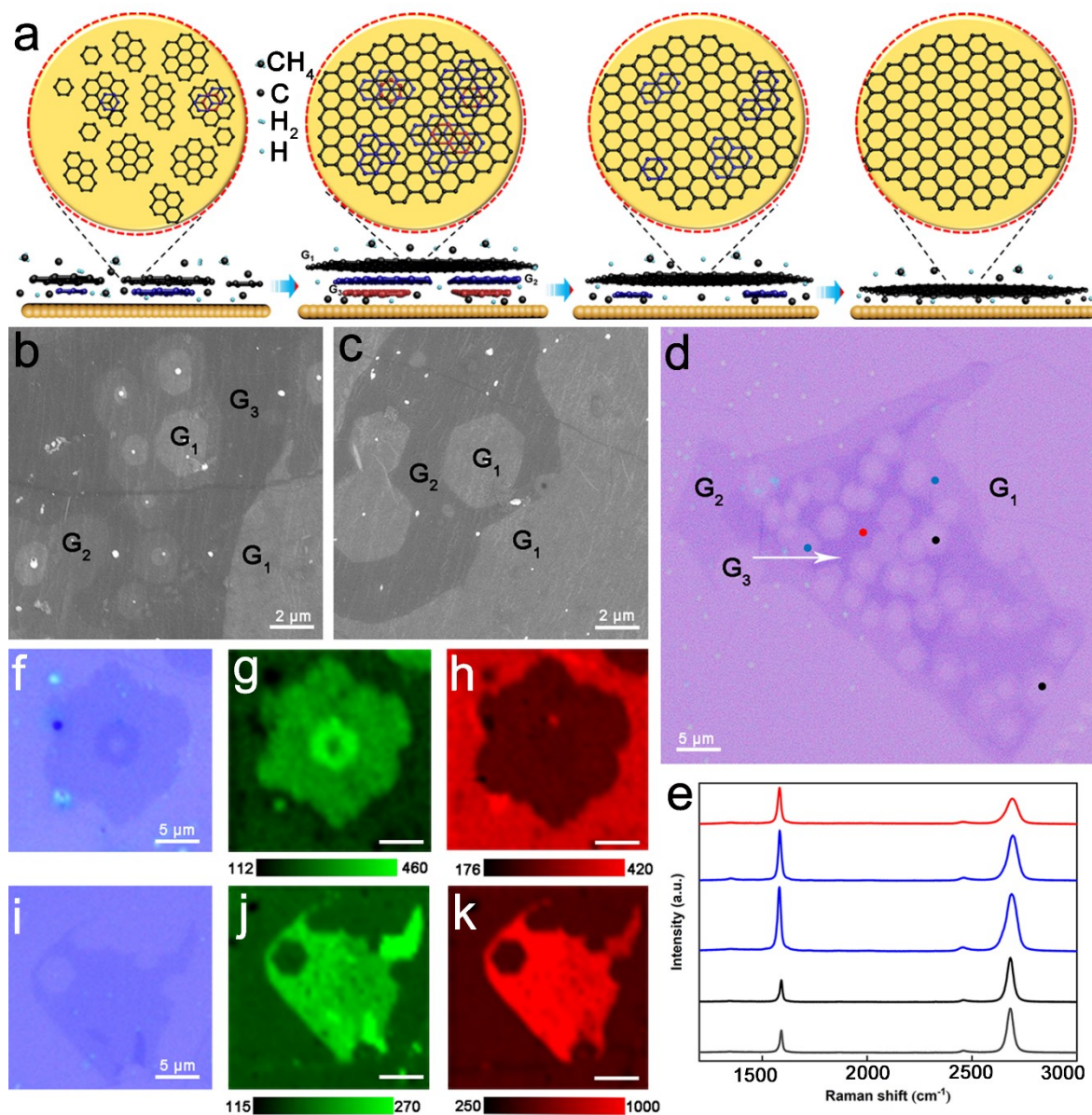


Figure 5. “Bottom-up-etching” of multi-layered graphene. (a) Schematic illustration of multi-layered graphene film growth and etching process for the preparation of uniform monolayer graphene. The first, second and third layers are shown in black, blue and red color, respectively. G₁, G₂ and G₃ indicate the graphene layers from top to down, respectively. Typical SEM (b, c) and optical images (d) of transferred graphene films on SiO₂/Si substrates, showing that the etching of multi-layered graphene occurs at the second etching stage. (e) Raman data of different locations marked in image d. Optical image (f) of etched multi-layered graphene on SiO₂/Si substrates, and the

This article is protected by copyright. All rights reserved.

corresponding Raman mappings (g, h) for G and 2D peak intensities, respectively. (i–k) Another case similar to the (f–h).

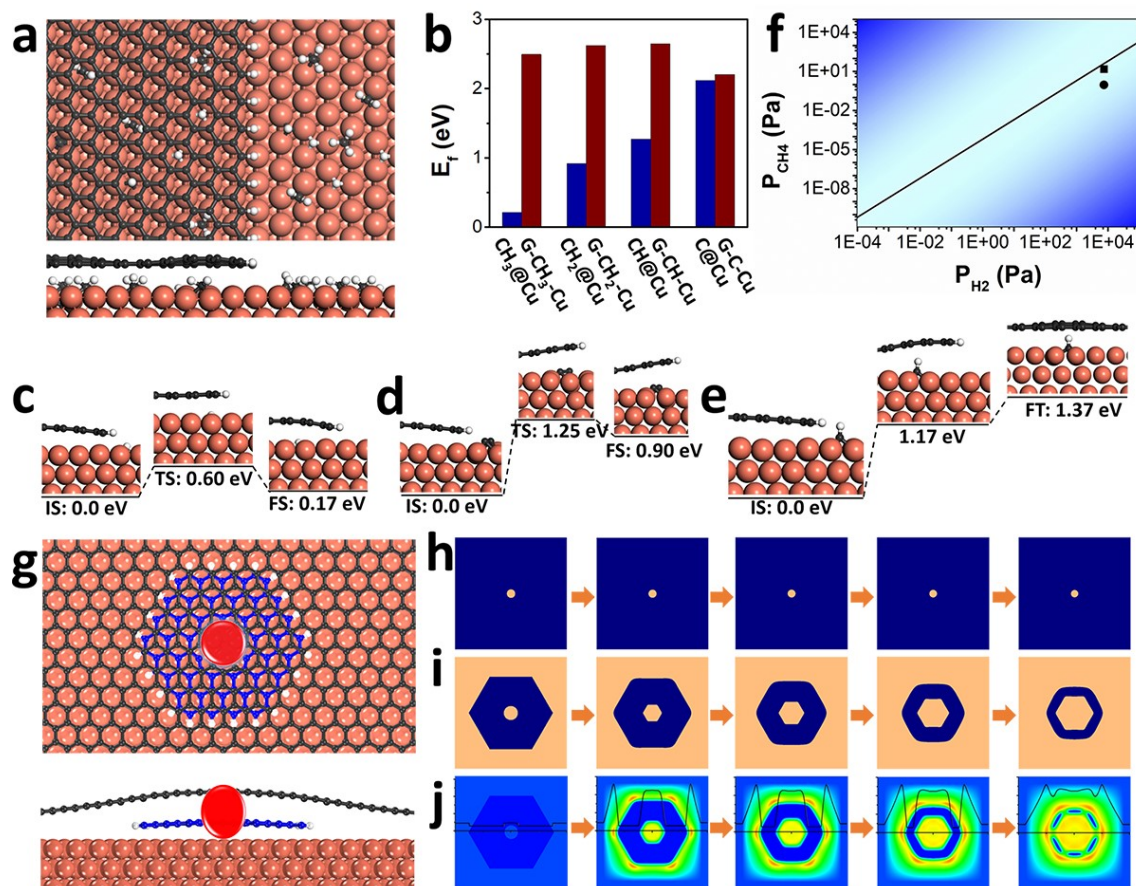


Figure 6. Theoretical exploration on the synthesis of monolayer graphene by growth and selective etching. (a) Atomic schematics showing the distribution of CH_i ($i = 0, 1, 2$ and 3) radicals and H atoms on a bare $\text{Cu}(111)$ surface and at the interface between graphene and Cu substrate. (b) Formation energies of CH_i ($i = 0, 1, 2$ and 3) radicals on a bare $\text{Cu}(111)$ surface (denoted by $\text{CH}_i@Cu$) and at the graphene-Cu interface (denoted by $G\text{-CH}_i\text{-Cu}$). (c, d and e) Calculated diffusion barriers of a H atom, C_2 and CH_3 radical from the bare $\text{Cu}(111)$ surface to the graphene-Cu interface. IS, TS and FS represent initial state, transition state and final state, respectively. (f) Predicted diagram on the growth (above the black line) and etching (below the black line) condition of the top-layer graphene on $\text{Cu}(111)$ surface at 1300 K. Square and circular dots denote the typical growth and selective etching conditions in our experiment, respectively. (g) Schematics showing the initial structure of CVD grown graphene monolayer with one bottom-layer nucleated at an impurity particle (large red sphere) and grown beneath the continuous graphene top-layer, prior to the selective etching step.

This article is protected by copyright. All rights reserved.

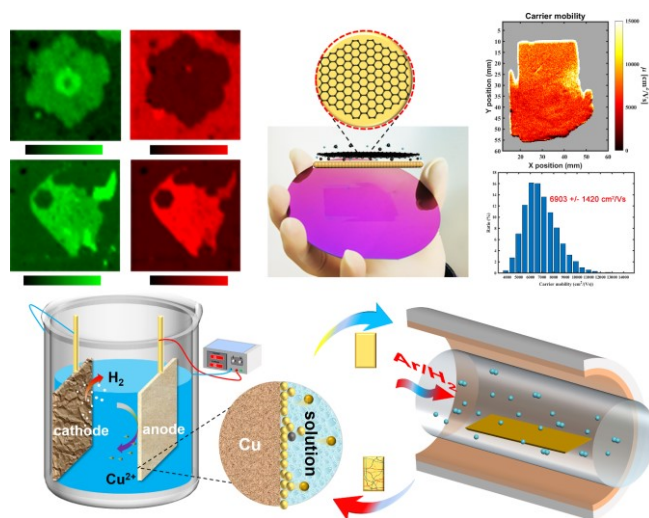
(h–j) Simulated selective etching process of the structure shown in (g). (h, i) show the evolution of the graphene top-layer and bottom-layer during etching, respectively. (j) shows the evolution of concentration distribution of carbon precursors on Cu surface during etching. The concentration profiles along the black line are provided.

We report for the first time a cyclic electrochemical polishing and thermal annealing approach that allows the effective conversion from commercial Cu to single-crystal Cu(111) foils. Using the Cu(111), a general “bottom-up-etching” method is developed for producing pure monolayer graphene film with high electronic quality. This work provides new ways and mechanisms for these key issues.

Keyword: single-crystal Cu(111), monolayer graphene, chemical vapor deposition, grain boundary migration, etching

Wenqian Yao^{1,2,†}, Jianing Zhang^{1,2,†}, Jie Ji³, He Yang¹, Binbin Zhou⁴, Xin Chen³, Peter Bøggild³, Peter U Jepsen⁴, Jilin Tang⁵, Fuyi Wang⁵, Li Zhang⁶, Jiahui Liu⁶, Bin Wu^{1,*}, Jichen Dong^{1,*}, and Yunqi Liu^{1,2,*}

Bottom-Up-Etching Mediated Synthesis of Large-Scale Pure Monolayer Graphene on Cyclic-Polishing-Annealed Cu(111)



This article is protected by copyright. All rights reserved.